

High-resolution spatial reconstruction of cellular force-generating domains using physical constraints and rotationally invariant L^1 regularization

Joshua C. Chang¹, Yanli Liu², and Tom Chou^{2,3}

¹*Epidemiology and Biostatistics Section, Rehabilitation Medicine,
Clinical Center, The National Institutes of Health, Bethesda MD, 20892*
²*Dept. of Mathematics, UCLA, Los Angeles, CA 90095-1555 and*
³*Dept. of Biomathematics, UCLA, Los Angeles, CA 90095-1766*

We develop a method to reconstruct, from measured displacements of an underlying elastic substrate, the spatially dependent forces that cells or tissues impart on it. Given newly available high-resolution methods to image substrate displacements, it is desirable to be able to reconstruct small scale, compactly supported focal adhesions, which are localized and can exist only within the footprint of the cell or tissue. We solve this inverse problem using methods of convex regularization. In addition to the standard quadratic data mismatch terms that defines least-squares fitting, we motivate a term in the objective function which penalizes variations in the vectorial invariants of the reconstructed surface stress while preserving boundaries. By minimizing the objective function subject to appropriate physical constraints, we are able to efficiently reconstruct stress fields with localized structure from simulated and experimental substrate displacements. We provide a numerical method for setting up a discretized inverse problem that is solvable by standard convex optimization techniques. Our method incorporates the exact solution for the stress tensor accurate to first-order finite-differences and motivates the use of distance-based cutoffs for data inclusion and problem sparsification.

PACS numbers:

INTRODUCTION

The adhesion of cells and tissues to their environment has profound consequences on processes such as cell polarization [1], division, differentiation [2], tissue morphology during development [3], wound healing [4–6], and cancer metastasis [7]. Hence, quantifying how cells attach to an impart force on the surrounding material is an important technical challenge in cell biology.

Cell motility and response to signals have hitherto typically been studied in two-dimensional geometries in which cells are placed on a flat elastic substrate. Dynamic adhesion between the cells and the substrate are realized through *e.g.*, lamellapodia, filapodia, and dynamically reorganizing focal adhesions [8]. Such structures are spatially localized, as shown in Fig. 1. Similarly, on larger length scales, a collection of cells can give rise to localized stress distributions. For example, the leading edge of a cell layer produces the pulling force that leads to migration in wound healing assays.

Dynamically varying force-generating structures are often small and difficult to image, especially without biochemical modification such as incorporation of fluorescent dyes. Therefore, other methods for inferring their positions and magnitudes have been developed. Methods using deformation of pillar structures [9] or textured substrates have been developed [10]. These methods require the cell to attach to a nonflat interface. The simplest method compatible with a flat interface relies on measuring the displacement of fiduciary markers, such as gold nanoparticles, embedded in the elastic substrate [11]. The measured displacements are an indirect probe of the

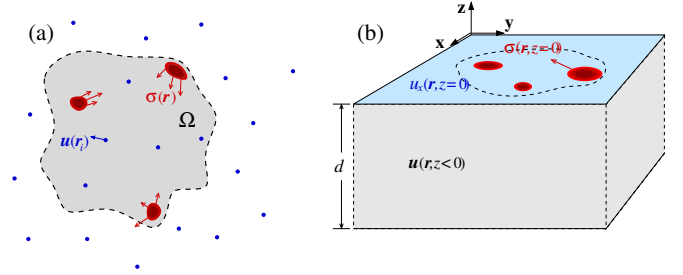


FIG. 1: A schematic of an isolated cell. (a) The boundary of the cell footprint is denoted by the dashed curve, the support of the stress field is represented by the red regions that impart a stress $\mathbf{f}(x, y)$ on the surface. Displacements $\mathbf{u}(\mathbf{r}_i)$ of the elastic medium are measured at position $\mathbf{r}_i = x_i \hat{x} + y_i \hat{y} + z_i \hat{z}$ (blue dots) that can be inside or outside the cell footprint, on the surface ($z_i = 0$), or below the surface ($z_i < 0$). (b). A perspective view of the elastic substrate and cellular footprint.

force-generating structures, *e.g.*, focal adhesions. Any inversion method should be able to not only reconstruct the positions and magnitudes of the stress field, but should ideally be able to capture potentially sharp boundaries of the stress-generating structures. However, fiduciary markers embedded in the 3D substrate are typically too sparse to reveal a displacement field with sufficient resolution to infer small cellular focal adhesion structures. To image such subcellular stress structures, high resolution reconstructions are required [12]. Experimentally, a new high-resolution imaging method has been developed using $9\mu\text{m}$ -period grid patterning of the substrate [13]. A surface grid pattern of fluorescent adhesion proteins

allows surface deformation to be directly measured using conventional microscopes.

In light of such higher spatial resolution techniques, we develop a novel method for elastic stress source recovery using ideas developed for image segmentation [14]. This class of methods relies on optimization that uses an L^1 regularization term in the objective function [15]. This type of regularization term is not derived from any fundamental physical law, but represents a prior knowledge that the function to be recovered is sparse in content except near edges. In addition, the overall objective function will be constructed to obey physical constraints and symmetries.

In the next section, we review the standard linear equations of elasticity that describe the displacement field as a function of an arbitrary surface stress distribution. This model is then used to construct the data mismatch term in the objective function. We then motivate regularization and constraint terms in the full objective function. Finally, we demonstrate our method using both simulated and experimental data. Our method provides good reconstruction of localized structures that exhibit desirable qualities such as the suppression of Gibbs ringing phenomenon at the boundaries of the stress structures.

ELASTIC MODEL

We first derive the linear elastic Green's function associated with a point force applied to the surface of a semi-infinite half-space, as shown in Fig. 1(b). We assume that the elastic medium is infinite in both depth ($d \rightarrow \infty$) and lateral extent. The Green's function tensor defined in the domain $\mathcal{D} = \{(x, y, z) | x, y \in \mathbb{R}, z \leq 0\}$ is given by

$$\mathbf{G} = \begin{bmatrix} G_{xx}(x, y, z) & G_{xy}(x, y, z) & G_{xz}(x, y, z) \\ G_{yx}(x, y, z) & G_{yy}(x, y, z) & G_{yz}(x, y, z) \\ G_{zx}(x, y, z) & G_{zy}(x, y, z) & G_{zz}(x, y, z) \end{bmatrix} \quad (1)$$

where the components are explicitly given in Appendix A. For example,

$$G_{sz,zs}(x, y, z) = \frac{1 + \nu}{2\pi E} \left(\frac{sz}{R_\perp^3} \pm \frac{(1 - 2\nu)s}{R_\perp(R_\perp - z)} \right). \quad (2)$$

where $s \equiv x, y$. The equation with \pm corresponds to G_{sz} and G_{zs} , respectively, and $R_\perp \equiv \sqrt{x^2 + y^2}$. The Young's modulus and Poisson ratio of the elastic substrate are denoted by E and ν , respectively. For Matrigel, $E \approx 4 \pm 3 \times 10^2$ Pa and $\nu \approx 0.5$ [16]. Throughout the rest of this manuscript, we will express stress in units of E . The displacement of a material point at $(x, y, z \leq 0)$ in the medium due to a stress distribution \mathbf{f} is simply the convolution $\mathbf{u}(\mathbf{r}) \equiv [u_x \ u_y \ u_z]^\top = \mathbf{G} * \mathbf{f}$.

For our specific problem, we shall restrict the forces to surface stresses \mathbf{f} that act on the plane perpendicular to

the \hat{z} axis. We define the in-plane stress distribution, at depth z , as $\mathbf{f}(x, y) = f_x(x, y)\hat{x} + f_y(x, y)\hat{y}$. The resulting surface-level displacement fields become

$$u_s(x, y, z) = \sum_{k=x,y,z} \int_{\Omega} dx' dy' G_{sk}(x-x', y-y', z) f_k(x', y'). \quad (3)$$

Note that tangential stresses can induce displacements in the direction normal to the surface. For cells on flat surface, we assume that $f_z = 0$.

INVERSE PROBLEM

Next, we develop an objective function for which the minimizing solution provides a good approximation to the underlying stress field, while preserving discontinuities. The first component is simply a quadratic data mismatch term defined by the sum over the displacements measured at the N measurement positions at \mathbf{r}_i :

$$\Phi_{\text{data}}[\mathbf{f}] = \sum_i^N |\mathbf{u}^{\text{data}}(\mathbf{r}_i) - \mathbf{u}(\mathbf{r}_i|\mathbf{f})|^2. \quad (4)$$

Since $\mathbf{u}^{\text{data}}(\mathbf{r}_i)$ is given, and $\mathbf{u}(\mathbf{r}_i|\mathbf{f})$ is given by the linear model of Eq. 3, this contribution to the objective function is a functional over the surface force $\mathbf{f}(x, y)$. For simplicity, we will assume that the data points are measured only at the interface $z = 0$ over an uniform grid with coordinates given $\{(x_j, y_k) : j \in \{1, 2, \dots, J\}, k \in \{1, 2, \dots, K\}\}$.

In Eq. 3, we have restricted the domain of integration to lie within the cell footprint Ω , further emphasizing that $\mathbf{f}(x, y)$ has compact support. As a consequence of compact support, for a fixed, discretized approximation of $\mathbf{f}(x, y)$, the displacements can be obtained exactly by solving an equivalent system of linear equations of finite dimension.

Here, we explicitly define this system of linear equations given a piecewise-affine approximation of the stress field. Let us consider the first-order approximation of $f_x(x, y)$ and $f_y(x, y)$ using central finite differences, for $x \in [x_j - \delta x/2, x_j + \delta x/2] \cap y \in [y_j - \delta y/2, y_j + \delta y/2]$,

$$\begin{aligned} f_x(x, y) &= f_x(x_i, y_j) \\ &+ (x - x_i) \frac{f_x(x_{i+1}, y_j) - f_x(x_{i-1}, y_j)}{2\delta x} \\ &+ (y - y_j) \frac{f_x(x_i, y_{j+1}) - f_x(x_i, y_{j-1})}{2\delta y} \\ &+ \mathcal{O}(\delta x)^2 + \mathcal{O}(\delta y)^2, \end{aligned} \quad (5)$$

where i, j denotes a tuple of grid coordinates. In effect, we are performing sub-pixel interpolation of the stress

where the stress is fully-determined by its values at the grid vertices.

Upon using Eq. 5, we can rewrite Eq. 3 by decomposing the integral into a sum of integrals over grid cells. After further regrouping terms, we find a linear system of equations for $u_s(x, y)$ at all grid points simultaneously. For example,

$$u_x(x_n, y_m) = X^{nmjk} f_x(x_j, y_k) + Y^{nmjk} f_y(x_j, y_k), \quad (6)$$

where the tensors X^{nmjk} and Y^{nmjk} are given in Appendix B and summation notation for each index tuple (j, k) has been implicitly assumed.

From an equation-counting perspective, the system of equations is exactly determined given that one has at least as many measurement points as grid cells in the resolution that one wishes to reconstruct the stress field, provided that one is able to measure displacements in both principle directions. Even if one is able to measure both displacements, the problem may still be difficult since the inversion of Eq. 6 maybe highly ill-conditioned and the measurements are taken in the presence of noise at a finite precision. To resolve these issues, we introduce a number of physically consistent constraints and regularization terms relevant to this system.

Physical constraints and regularization

The remaining components of the objective function should contain information about the the known physical constraints as well as regularization terms that better condition the overall optimization problem. Various regularization terms have been motivated, but they can also be associated with prior knowledge on the solution [17].

First, we consider explicit physical constraints. Since we are assuming inertial effects are negligible, we require that the net force is zero, or that

$$\int_{\Omega} f_x(x, y) dx dy = \int_{\Omega} f_y(x, y) dx dy = 0. \quad (7)$$

Likewise, we require that there is no net torque, or that

$$\int_{\Omega} x f_y(x, y) dx dy = \int_{\Omega} y f_x(x, y) dx dy. \quad (8)$$

Another physical constraint is the requirement that surface stress at locations outside of the cell footprint vanish. In regions where there is no contact between the cell and the substrate, no mechanism can impart stress. Thus, the stress field is compactly supported within the cell footprint. The stress field may be further localized through cellular focal adhesions within the cell footprint

To better condition the inference of $\mathbf{f}(x, y)$, we regularize this problem by forcing the reconstruction to obey some physically relevant characteristics of the surface

stress. In many other types of inverse problems, for example, in the inference of the potential of mean force of a molecular bond, a constraint on differentiability is typically imposed on the function to be inferred [18]. A typical constraint of this nature may be a quadratic penalty on the gradients of the function to be inferred. However, such L^2 functional regularization often leads to ringing and inaccurate functional reconstruction especially when the underlying function is highly localized or compactly supported.

Thus, L^1 regularization on the function or on its variations have been developed. These approaches are suitable for problems such as segmentation of images where boundaries are sharp [15]. In these problems, the data is sparse in the sense that definition of boundaries in an image contain most of the information. Likewise, in the stress recovery problem at hand, the data consisting of displacements at a finite number of measurement positions may be considered sparse.

To this end we employ a variant of a penalty used often in image processing applications, where one penalizes the L^1 norm of the variation in the fields, or the total variation. In analogy with image processing, one might choose regularization terms Φ_{reg} of the form

$$\Phi_{L^1} = \int_{\Omega} (|f_x(x, y)| + |f_y(x, y)|) d\mathbf{r}, \quad (9)$$

$$\Phi_{\text{TV}_1} = \int_{\Omega} (|\nabla f_x(x, y)| + |\nabla f_y(x, y)|) d\mathbf{r} \quad (10)$$

and

$$\Phi_{\text{TV}_2} = \int_{\Omega} (|\partial_x f_x| + |\partial_y f_x| + |\partial_x f_y| + |\partial_y f_y|) d\mathbf{r}, \quad (11)$$

representing an L^1 regularization of the surface stress and two forms of its total variation, respectively. Since these regularization terms are not based on any fundamental physical law, there is some freedom in choosing their form. However, we do not want rotational anisotropy in the measurement grid to affect the final result. The regularization terms should not induce any additional anisotropy over that of the displacement field. Thus, appropriate regularizations should be invariant under coordinate rotation. The coordinate-independent regularizer can be constructed from the magnitude of the force vector at the surface

$$|\mathbf{f}(x, y)| = \sqrt{f_x^2 + f_y^2}. \quad (12)$$

Any regularization penalty imposed on the reconstruction problem must be a functional of these invariants in order to maintain rotational invariance relative to the choice of how the displacements are sampled. In this manuscript, for simplicity, we will focus on regularizers

$\Phi_{\text{reg}} = \tilde{\Phi}_{\text{reg}}$ that are functions of the magnitude and trace; for example

$$\tilde{\Phi}_{L^1} = \int_{\Omega} |\mathbf{f}(x, y)| dx dy \quad (13)$$

and

$$\tilde{\Phi}_{L^2} = \int_{\Omega} |\mathbf{f}(x, y)|^2 dx dy. \quad (14)$$

Using either of these expressions as the regularization norm suggests the penalized optimization problem

$$\hat{\mathbf{f}}|\lambda = \arg \min_{\mathbf{f}} \{ \Phi_{\text{data}}[\mathbf{f}] + \lambda \Phi_{\text{reg}}[\mathbf{f}] \}, \quad (15)$$

subject to the no-force, no-torque, and footprint constraints (Eqs. 7 and 8) on \mathbf{f} mentioned above. In Eq. 15, $\lambda > 0$ is a tunable parameter. This problem is in a standard form that is directly solvable using a variety of optimization routines. In our implementation, we use a second-order quadratic cone solver [?].

To reduce the size of the system of equations described in Eqs. 6, we note that the Green's function falls off at a rate of $|\mathbf{r}|^{-1}$. However, when combined with the zero-force constraint, the relationship between the displacements and the support of the stress field falls off at the much quicker rate of $|\mathbf{r}|^{-2}$. Formally, if $\Omega = \text{sup}(\boldsymbol{\sigma}) \subset \mathbb{R}^2$ is compact, and $\int \boldsymbol{\sigma}(\mathbf{r}) d\mathbf{r} = \mathbf{0}$, then as $\mathbf{r} \rightarrow \infty$, $u_{x,y}(\mathbf{r}) = \mathcal{O}(|\mathbf{r}|^{-2})$.

The decay of the influence of stress on the system provides justification for setting distance-based cut-offs of the linear system. The effect of the cut-off is to limit the left-hand side of Eq. 6 to locations only within some maximal distance R_{\perp} from the outline of the cell.

RESULTS

We implemented our regularized inversion method in Python version 3.5, where optimization is performed using the `cvxpy` package with the `ecos` solver. Our implementation is available at <https://github.com/joshchang/tractionforce>.

First, we tested our method on simulated data derived from a force- and torque-free test stress field shown in Fig. 2. The test pattern consists of four separated circular stress pads, or focal adhesions, with radii $r_1 = 1/5$, $r_2 = 1/6$, $r_3 = 1/8$, and $r_4 = 1/4$, and centers at positions $(x_1, y_1) = (-1, -1/2)$, $(x_2, y_2) = (0, -1)$, $(x_3, y_3) = (2, 1)$, and $(x_4, y_4) = (0, 1)$. The pads 2,3, and 4 are connected in a triangle as shown, while pad 1 is connected only to pad 2. The tensions along these connections give rise to surface stresses imparted by the pads onto the substrate. We will assume that the stress fields in pads 1,2, and 3 are uniformly distributed within the circular disks. For pad 4, we assume that the filaments connected

to it distributed according to a cone-like density function. Thus, the stress field within pad 4 linearly decrease along the radial direction. The stresses $\mathbf{f}^{(i)}$ under each patch i are decomposed into contributions arising from the total tension T_{ij} connecting them with pad j and can be expressed in the form

$$\mathbf{f}^{(1)} = a_{12} \left(\hat{x} - \frac{\hat{y}}{2} \right) \quad (16)$$

$$\mathbf{f}^{(2)} = \frac{G_4}{A_2} \hat{y} - a_{12} \frac{A_1}{A_2} \left(\hat{x} - \frac{\hat{y}}{2} \right) + a_{23} (\hat{x} + \hat{y}) \quad (17)$$

$$\mathbf{f}^{(3)} = -\hat{x} \frac{G_4}{A_3} - a_{23} \frac{A_2}{A_3} (\hat{x} + \hat{y}) \quad (18)$$

$$\mathbf{f}^{(4)} = g_4 \left(1 - \frac{r}{r_4} \right) (\hat{x} - \hat{y}) \quad (19)$$

where $a_{12}, a_{23}, g_4 > 0$ are constant amplitudes, $A_i = \pi r_i^2$ are the pad areas, and

$$G_4 = 2\pi g_4 \int_0^{r_4} \left(1 - \frac{r}{r_4} \right) r dr = \frac{g_4 \pi r_4^2}{3} \quad (20)$$

is the total force on pad 4 in each direction. Note that both test stress fields are constructed to be force- and torque-free. We first generate the displacement fields using the Green's function (*i.e.*, Eq. 3 for surface values $\mathbf{u}(x, y, z = 0)$) and then recover $\mathbf{f}(\mathbf{r})$ from these displacements.

Figure 3 compares the reconstruction achieved from using the different forms of Φ_{reg} . In all of these reconstructions, we have imposed that the surface stress is both force-free and torque-free, and also that the support of the stress is within given cell boundaries. We see that all forms of regularization recover the signal due to the four pads. The reconstruction using the isotropic L^1 penalty is seen to be more sparse than that of the isotropic L^1 penalty.

The adjustable parameter λ was chosen in each instance by examining the balance between data mismatch and regularity using trade-off curves shown in Supplemental Fig. 11, and taking the value for λ that yields a point farthest away from the line segment joining the ends of the plot. In Fig. 11, the chosen value of λ corresponds to the given balance between regularity and data fidelity marked by the red circle. The solution corresponding to this particular value of λ is shown in Fig. 3. Each row in Fig. ?? corresponds to the use of a different regularization penalty functional.

Figure 4 shows reconstructions of the 4-pad test patterns using $\tilde{\Phi}_{L^1}$ as a function of the coarseness of the displacement data. The general features of the stress patterns are preserved under coarsening but sufficient den-

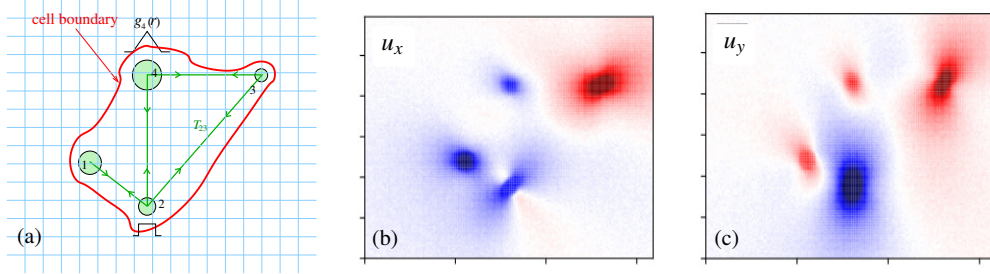


FIG. 2: **Test stress fields and surface displacements.** (a) Four focal adhesions attached by filaments indicated by the green lines. The red border represents the extent of the cell footprint and can be determined experimentally as part of the imaging. Mathematically, the cell boundary forms the basis for a constraint on the stress distribution and we explore the dependence of the quality of reconstruction on the footprint constraint. The faint blue grid represents the regular points at which displacements might be measured. (b) and (c) show the corresponding surface displacements $u_x(x, y)$ and $u_y(x, y)$, respectively.

sity of data points are needed to resolve fine scale variations in the stress field. Here, we applied the boundary constraint corresponding to the cell footprints shown in Fig. 2(a).

We also test loss of information by assuming that displacements only in the \hat{x} or \hat{y} directions are measured. In Fig. 5 we show reconstructions using only u_x or u_y for both the annulus and 4-pad test patterns.

Next, we illustrate the effects of relaxing the no-force and no-torque constraints. Fig. 6 shows optimal- λ reconstructions using $\tilde{\Phi}_{L^1}$, but without force or torque constraints.

Finally, we explore the effects of relaxing the footprint constraint. By artificially expanding the footprint, we relax the constraint. In the 4-pad example, using the $\tilde{\Phi}_{L^1}$ regularizer, the footprint constraint is not especially critical. However, as we shall see, for stresses that are concentrated near the periphery of the cell footprint,

RECONSTRUCTION FROM SINGLE CELL DATA

To apply our method on high-resolution experimental data, we consider the displacements resulting from stress generated by a single isolated mesenchymal stem cell. The surface displacements were measured using Hilbert space dynamometry which uses phase information of the periodic signal arising from a chemically patterned grid on the substrate [13]. In this dataset only x -displacements at a resolution of the patterned grid spacing can be measured, as shown in Fig. 8

The λ -optimal results for the reconstructed stress field $\hat{\mathbf{f}}$ using the $\tilde{\Phi}_{L^1}$ regularization and the full set of constraints are shown in Fig. 9.

As evident from the reconstructions, the surface forces are concentrated near the border of the cell footprint. For such boundary-dominated stress fields, the footprint constraint is expected to be important in the recovery of

f. Fig. 10 compares the reconstruction with that computed with an artificially expanded footprint. Using an incorrect footprint results in a force distribution $\hat{\mathbf{f}}$ that differs from the “true” distribution, especially near the borders.

SUMMARY AND CONCLUSIONS

We presented a systematic approach to solving the inverse problem associated with the reconstruction—from displacements of the underlying substrate—of surface stresses imparted by isolated cells. Under piecewise affine approximations of the surface force, we provided an exact solution to the forward problem as a system of linear equations. This approximation to the forward problem is used in a data mismatch term Φ_{data} (Eq. 4). In the numerical implementation of the optimization problem, we also motivated the use of a cut-off in the solution of the forward problem that greatly reduces the rank of the inverse problem thereby decreasing both the computational complexity of the problem and the memory requirements. This cut-off approach is appropriate only in scenarios in which the stress-generating cell is localized and far from the system boundaries. Assays in which cells or layers that extend to the boundary of the sample, or in which the substrate is of finite depth will require the careful implementation of boundary conditions defined by the sample size.

Upon further consideration of physical and geometric features, we motivated additional important terms the objective function. The fundamental optimization problem involves minimizing an objective function containing L^1 regularization terms that are invariant to coordinate rotation. The anisotropy of $\hat{\mathbf{f}}$ derives solely from the anisotropy in the data. Important physical constraints including vanishing net force/net torque and zero stress outside the cell footprint are also imposed. By exploring

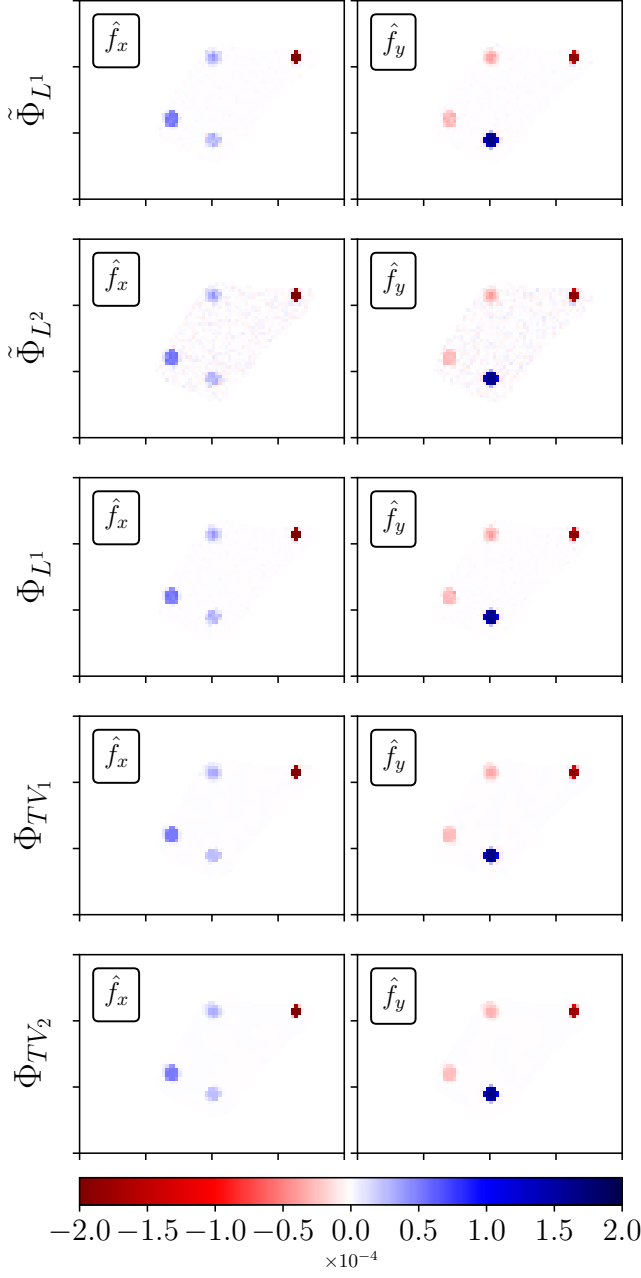


FIG. 3: **Comparing different regularizers.** Reconstruction of the test patterns using the different forms of Φ_{reg} : Φ_{L^1} , Φ_{TV_1} , Φ_{TV_2} , $\tilde{\Phi}_{L^1}$ and $\tilde{\Phi}_{L^2}$. Regularization parameters chosen as in Fig. 11.

the mathematical features of the stress inference problem, we find that properly identifying and implementing physical constraints (such as no-force and no-torque) are key to accurate stress recovery.

We also showed how the known footprint boundary can impact the reconstruction, especially when adhesion sites are concentrated near the cell boundary. Such focal adhesion configurations are commonly observed in cells

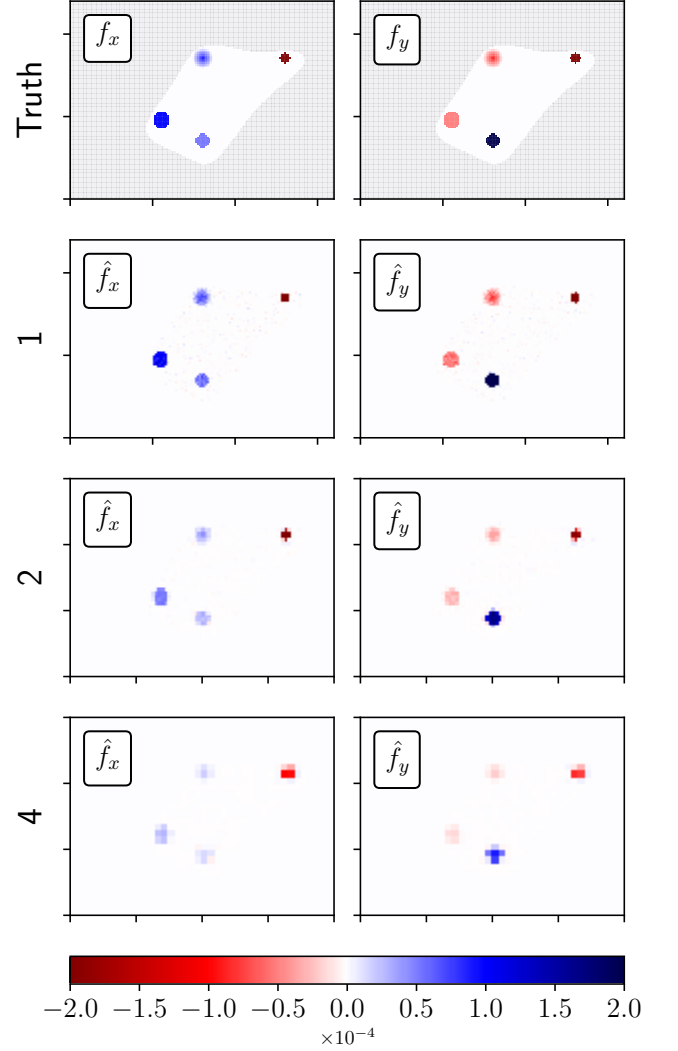


FIG. 4: **Grid coarsening.** Using every $n \in \{1, 2, 4\}$ lattice points of observations. The reconstruction is also performed at the same resolution. In general, the optimization is stable and the qualitative features of the reconstructed $\mathbf{f}(x, y)$ are robust to modest data coarsening.

grown on 2D substrates. In general, cell boundaries that artificially extend beyond the true footprint worsens the inversion, allowing for “leakage” of stress beyond its actual support.

ACKNOWLEDGEMENTS

This work was supported in part by the Intramural Research Program of the NIH.

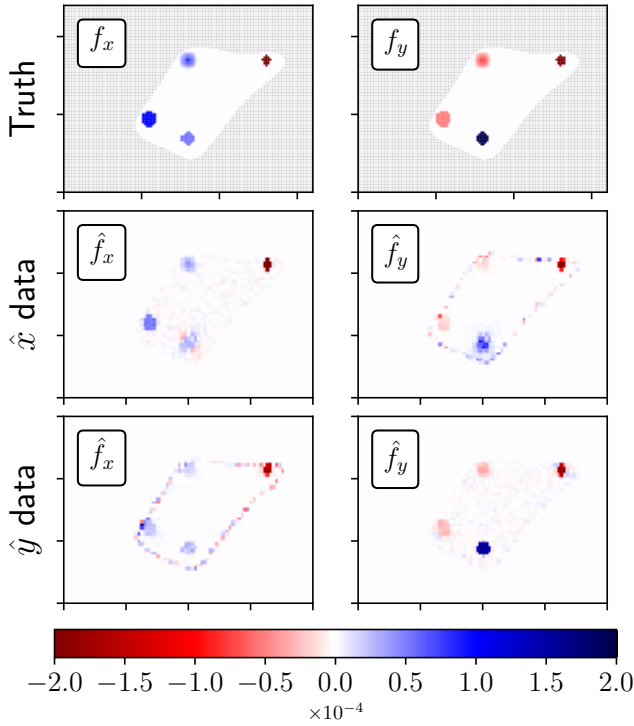


FIG. 5: **Unidirectional displacement measurements**, where displacements are only measured along a single axis, may be used for reconstruction. Reconstructions of both components of the four-pad surface stress shown under measures along only \hat{x} or only \hat{y} , using the $\tilde{\Phi}_{L^1}$ norm.

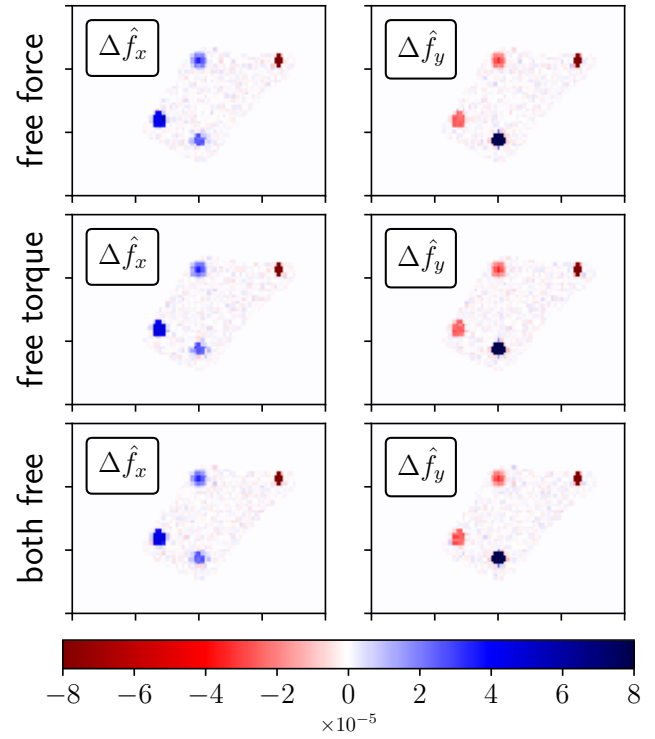


FIG. 6: **Constraints are unsatisfied unless enforced**. Plotted are best reconstructions under $\tilde{\Phi}_{L^1}$ penalty and the difference between these reconstructions and the corresponding fully constrained reconstruction in Fig. 3.

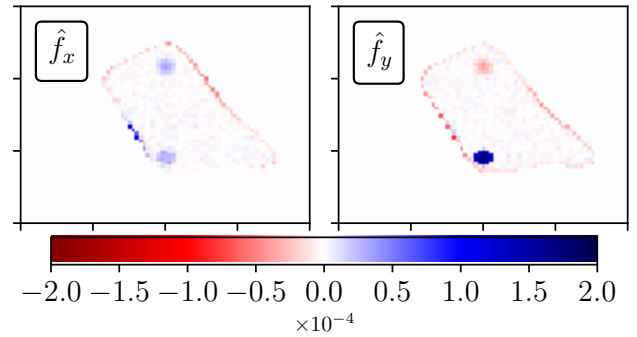


FIG. 7: **Footprint misspecification**. Reconstructions performed under footprint drawn in an incorrect orientation.

- [1] M. Prager-Khoutorsky, A. Lichtenstein, R. Krishnan, K. Rajendran, A. Mayo, Z. Kam, B. Geiger, and A. D. Bershadsky, *Nature Cell Biology* **13**, 1457 (2011).
- [2] T. Pieters and F. van Roy, *Journal of Cell Science* **127**, 2603 (2014).
- [3] A. Aman and T. Piotrowski, *Developmental Biology* **341**, 20 (2010).
- [4] L. Schneider, M. Cammer, J. Lehman, S. K. Nielsen, C. F. Guerra, I. R. Veland, C. Stock, E. K. Hoffmann, B. K. Yoder, A. Schwab, et al., *Cell Physiology and Biochemistry* **25**, 279 (2010).
- [5] L. Li, Y. He, M. Zhao, and J. Jiang, *Burns and Trauma* **1**, 21 (2013).
- [6] M. Aragona, S. Dekoninck, S. Rulands, S. Lenglez, G. Mascré, B. D. Simons, and C. Blanpain, *Nature Communications* **8**, 14684 (2017).
- [7] A. G. Clark and D. M. Vignjevic, *Current Opinion in Cell Biology* **36**, 13 (2015).
- [8] J. Watson, B. Alberts, D. Bray, M. Raff, and J. Lewis, *Molecular Biology of the Cell*, 6th Edition (Garland Science, 2014).
- [9] J. L. Tan, J. Tien, D. M. Pirone, D. S. Gray, K. Bhadriraju, and C. S. Chen, *Proceedings of The National Academy of Sciences USA* **100**, 1484 (2003).
- [10] N. Q. Balaban, U. S. Schwarz, D. Riveline, P. Goichberg, G. Tzur, I. Sabanay, D. Mahalu, S. Safran, A. Bershad-

- sky, L. Addadi, et al., *Nature Cell Biology* **3**, 466 (2001).
- [11] J. H.-C. Wang and J.-S. Lin, *Biomechanics and Modeling in Mechanobiology* **6**, 361 (2007).
- [12] B. Sabass, M. L. Gardel, C. M. Waterman, and U. S. Schwarz, *Biophysical Journal* **94**, 207 (2008).
- [13] S. Sridharana, Y. Li, L. Foucarde, H. Majeed, B. Bhaduria, A. J. Levine, K. Kilian, and G. Popescu, *Nature Methods* (2017).
- [14] T. Goldstein and S. Osher, *SIAM J. Imaging Sciences* **2**, 323 (2009).
- [15] T. F. Chan and S. Esedoglu, *SIAM J. Appl. Math.* **65**,

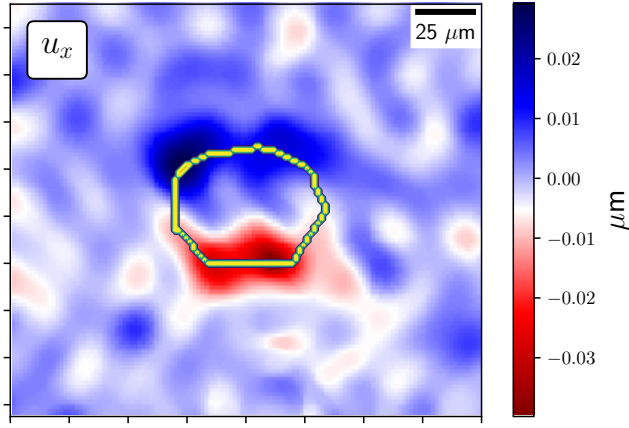


FIG. 8: **Mesenchymal stem cell displacement field.** Measured along \hat{x} (the horizontal axis). Boundary of the cell (yellow) was hand-drawn based on bright-field image of the cell.

- 1817 (2004).
- [16] S. S. Soofia, J. A. Lasta, S. J. Liliensieka, P. F. Nealey, and C. J. Murphy, *Journal of Structural Biology* **167**, 216 (2009).
 - [17] J. C. Chang, V. M. Savage, and T. Chou, *Journal of Statistical Physics* **157**, 582 (2014).
 - [18] J. C. Chang, P.-W. Fok, and T. Chou, *Biophysical Journal* **109**, 966 (2015).
 - [19] L. D. Landau and E. M. Lifshitz, *Theory of Elasticity* (Pergamon Press, Oxford, 1970).

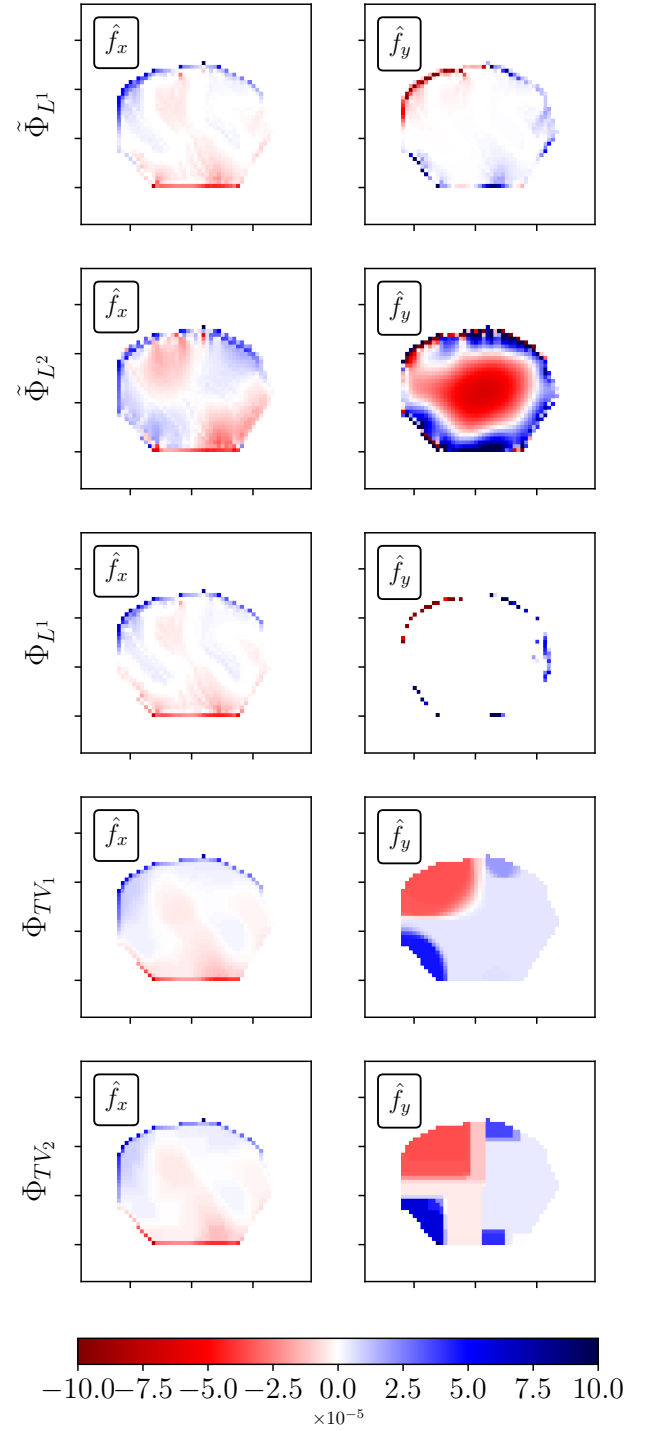


FIG. 9: **Reconstruction of experimental surface stress field.** Reconstruction of \mathbf{f} from the measured displacements shown in Fig. 8 using the norms defined in the manuscript. In each case, λ was chosen using the L-curve method as in the appendices.

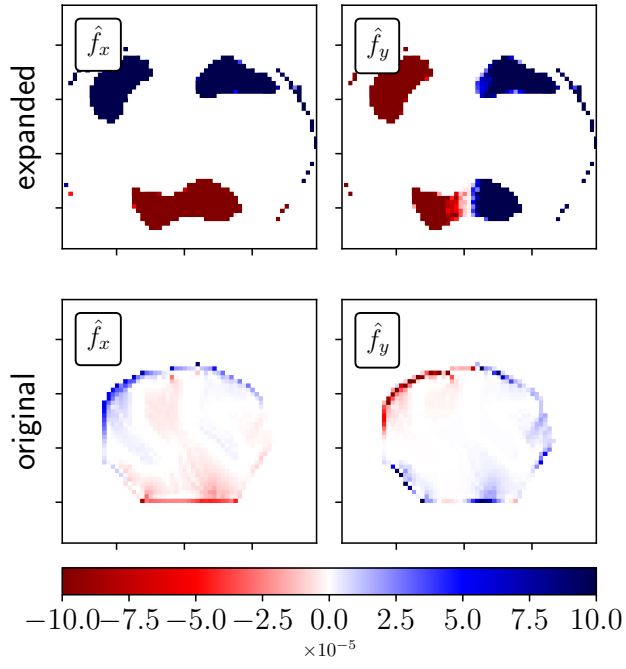


FIG. 10: **Modification of footprint constraint.** Comparing the surface force reconstruction using the estimated cell footprint (from the bright field image) with the reconstruction derived from a false cell footprint. Since the forces are concentrated near the cell border, the reconstruction is sensitive to the location of the border.

Appendix A: Elastic Green's function

For completeness, we explicitly list the components of the Green's tensor for a linear elastic substrate [19]

$$G_{ss}(x, y, z) = \frac{1+\nu}{2\pi E} \left[\frac{2(1-\nu)R_\perp - z}{R_\perp(R_\perp - z)} + \frac{[2R_\perp(\nu R_\perp - z) + z^2]s^2}{R_\perp^3(R_\perp - z)^2} \right], \quad (21)$$

$$G_{zz}(x, y, z) = \frac{1+\nu}{2\pi E} \left(\frac{2(1-\nu)}{R_\perp} + \frac{z^2}{R_\perp^3} \right), \quad (22)$$

$$G_{xy}(x, y, z) = G_{yx} = \frac{1+\nu}{2\pi E} \frac{[2R_\perp(\nu R_\perp - z) + z^2]xy}{R_\perp^3(R_\perp - z)^2}, \quad (23)$$

$$G_{sz, zs}(x, y, z) = \frac{1+\nu}{2\pi E} \left(\frac{sz}{R_\perp^3} \pm \frac{(1-2\nu)s}{R_\perp(R_\perp - z)} \right). \quad (24)$$

where $s \equiv x, y$. The last equation with \pm corresponds to G_{sz} and G_{zs} , respectively, and $R_\perp \equiv \sqrt{x^2 + y^2}$. The Young's modulus and Poisson ratio of the elastic substrate are denoted by E and ν , respectively.

Appendix B: Displacements and stresses at discrete positions

Here, we show the explicit expressions relating displacements $\mathbf{u}(x_n, y_m)$ at grid points (x_n, y_m) in terms of stress fields at the same locations. Using the interpolation of $\mathbf{f}(x, y)$ defined by Eq. 5 in Eq. 3, we find

$$\begin{aligned} u_x(x_n, y_m) = & \sum_{(x_j, y_k) \in \Omega} \left\{ \left[f_x(x_j, y_k) - x_j \left(\frac{f_x(x_{j+1}, y_k) - f_x(x_{j-1}, y_k)}{2\delta x} \right) - y_k \left(\frac{f_x(x_j, y_{k+1}) - f_x(x_j, y_{k-1})}{2\delta y} \right) \right] \langle G_{xx} \rangle^{nmjk} \right. \\ & + \left[\frac{f_x(x_{j+1}, y_k) - f_x(x_{j-1}, y_k)}{2\delta x} \right] \langle x G_{xx} \rangle^{nmjk} + \left[\frac{f_x(x_j, y_{k+1}) - f_x(x_j, y_{k-1})}{2\delta y} \right] \langle y G_{xx} \rangle^{nmjk} \\ & + \left[f_y(x_j, y_k) - x_j \left(\frac{f_y(x_{j+1}, y_k) - f_y(x_{j-1}, y_k)}{2\delta x} \right) - y_k \left(\frac{f_y(x_j, y_{k+1}) - f_y(x_j, y_{k-1})}{2\delta y} \right) \right] \langle G_{xy} \rangle^{nmjk} \\ & \left. + \left[\frac{f_y(x_{j+1}, y_k) - f_y(x_{j-1}, y_k)}{2\delta x} \right] \langle x G_{xy} \rangle^{nmjk} + \left[\frac{f_y(x_j, y_{k+1}) - f_y(x_j, y_{k-1})}{2\delta y} \right] \langle y G_{xy} \rangle^{nmjk} \right\}, \quad (25) \end{aligned}$$

where

$$\langle g(x, y) G_{uv} \rangle^{nmjk} = \int_{y_k - \delta y/2}^{y_k + \delta y/2} \int_{x_j - \delta x/2}^{x_j + \delta x/2} g(x', y') G_{uv}(x_n - x', y_m - y') dx' dy', \quad (26)$$

except that at the edges where we use one-sided differences so that we are only differentiating within Ω . A similar expression can be found for solving for u_y (not shown). Collecting terms, we write $u_{x,y}(x_n, y_m)$ in terms of $\mathbf{f}(x_j, y_k)$ in Eq. 6, where

$$\begin{aligned} X^{nmjk} = & \langle G_{xx} \rangle^{nmjk} - \langle G_{xx} \rangle^{n,m,j-1,k} \frac{x_{j-1}}{2\delta x} + \langle G_{xx} \rangle^{n,m,j+1,k} \frac{x_{j+1}}{2\delta x} - \langle G_{xx} \rangle^{n,m,j,k-1} \frac{y_{k-1}}{2\delta y} \\ & + \langle G_{xx} \rangle^{n,m,j,k+1} \frac{y_{k+1}}{2\delta y} - \frac{\langle x G_{xx} \rangle^{n,m,j-1,k}}{2\delta x} + \frac{\langle x G_{xx} \rangle^{n,m,j+1,k}}{2\delta x} - \frac{\langle y G_{xx} \rangle^{n,m,j,k-1}}{2\delta y} + \frac{\langle y G_{xx} \rangle^{n,m,j,k+1}}{2\delta y}, \quad (27) \end{aligned}$$

$$\begin{aligned}
Y^{nmjk} = & \langle G_{xy} \rangle^{nmjk} - \langle G_{xy} \rangle^{n,m,j-1,k} \frac{x_{j-1}}{2\delta x} + \langle G_{xy} \rangle^{n,m,j+1,k} \frac{x_{j+1}}{2\delta x} - \langle G_{xy} \rangle^{n,m,j,k-1} \frac{y_{k-1}}{2\delta y} \\
& + \langle G_{xy} \rangle^{n,m,j,k+1} \frac{y_{k+1}}{2\delta y} - \frac{\langle xG_{xy} \rangle^{n,m,j-1,k}}{2\delta x} + \frac{\langle xG_{xy} \rangle^{n,m,j+1,k}}{2\delta x} - \frac{\langle yG_{xy} \rangle^{n,m,j,k-1}}{2\delta y} + \frac{\langle yG_{xy} \rangle^{n,m,j,k+1}}{2\delta y}. \quad (28)
\end{aligned}$$

Explicit closed-form expressions for the integrals in Eq. 26 are given below. By defining $\Delta x_{nj}^+ = x_n - (x_j + \delta x/2)$, $\Delta x_{nj}^- = x_n - (x_j - \delta x/2)$, $\Delta y_{mk}^+ = y_m - (y_k + \delta y/2)$, and $\Delta y_{mk}^- = y_m - (y_k - \delta y/2)$, we find

$$\langle G_{uv} \rangle^{nmjk} = g_{uv}(\Delta x_{nj}^+, \Delta y_{mk}^+) - g_{uv}(\Delta x_{nj}^+, \Delta y_{mk}^-) - g_{uv}(\Delta x_{nj}^-, \Delta y_{mk}^+) + g_{uv}(\Delta x_{nj}^-, \Delta y_{mk}^-) \quad (29)$$

where

$$g_{xx}(x, y) = \frac{\nu+1}{\pi E} \left[x(1-\nu) \log \left(\sqrt{x^2+y^2} + y \right) + y \log \left(\sqrt{x^2+y^2} + x \right) - y \right] \quad (30)$$

$$g_{yy}(x, y) = \frac{\nu+1}{\pi E} \left[y(1-\nu) \log \left(\sqrt{x^2+y^2} + x \right) + x \log \left(\sqrt{x^2+y^2} + y \right) - x \right] \quad (31)$$

$$g_{xy}(x, y) = -\frac{\nu(\nu+1)}{\pi E} \sqrt{x^2+y^2}. \quad (32)$$

The first moments are

$$\begin{aligned}
\langle xG_{xx}(x, y) \rangle^{nmjk} = & \left[g_{xx}(\Delta x_{nj}^+, \Delta y_{mk}^+) - g_{xx}(\Delta x_{nj}^+, \Delta y_{mk}^-) - g_{xx}(\Delta x_{nj}^-, \Delta y_{mk}^+) + g_{xx}(\Delta x_{nj}^-, \Delta y_{mk}^-) \right] x_n \\
& - \left[g_{xx}^x(\Delta x_{nj}^+, \Delta y_{mk}^+) - g_{xx}^x(\Delta x_{nj}^+, \Delta y_{mk}^-) - g_{xx}^x(\Delta x_{nj}^-, \Delta y_{mk}^+) + g_{xx}^x(\Delta x_{nj}^-, \Delta y_{mk}^-) \right], \quad (33)
\end{aligned}$$

where

$$g_{xx}^x(x, y) = \frac{\nu+1}{2\pi E} \left[(\nu+1)y\sqrt{x^2+y^2} - (\nu-1)x^2 \log \left(\sqrt{x^2+y^2} + y \right) \right], \quad (34)$$

$$\begin{aligned}
\langle yG_{xx}(x, y) \rangle^{nmjk} = & \left[g_{xx}(\Delta x_{nj}^+, \Delta y_{mk}^+) - g_{xx}(\Delta x_{nj}^+, \Delta y_{mk}^-) - g_{xx}(\Delta x_{nj}^-, \Delta y_{mk}^+) + g_{xx}(\Delta x_{nj}^-, \Delta y_{mk}^-) \right] y_m \\
& - \left[g_{xx}^y(\Delta x_{nj}^+, \Delta y_{mk}^+) - g_{xx}^y(\Delta x_{nj}^+, \Delta y_{mk}^-) - g_{xx}^y(\Delta x_{nj}^-, \Delta y_{mk}^+) + g_{xx}^y(\Delta x_{nj}^-, \Delta y_{mk}^-) \right], \quad (35)
\end{aligned}$$

where

$$g_{xx}^y(x, y) = \frac{\nu+1}{2\pi E} \left[y^2 \log \left(\sqrt{x^2+y^2} + x \right) - \sqrt{x^2+y^2} \left((2\nu-1)x + \frac{1}{2}\sqrt{x^2+y^2} \right) \right], \quad (36)$$

and

$$\begin{aligned}
\langle xG_{xy}(x, y) \rangle^{nmjk} = & \left[g_{xy}(\Delta x_{nj}^-, \Delta y_{mk}^+) - g_{xy}(\Delta x_{nj}^-, \Delta y_{mk}^-) - g_{xy}(\Delta x_{nj}^+, \Delta y_{mk}^+) + g_{xy}(\Delta x_{nj}^+, \Delta y_{mk}^-) \right] x_n \\
& - \left[g_{xy}^x(\Delta x_{nj}^+, \Delta y_{mk}^+) - g_{xy}^x(\Delta x_{nj}^+, \Delta y_{mk}^-) - g_{xy}^x(\Delta x_{nj}^-, \Delta y_{mk}^+) + g_{xy}^x(\Delta x_{nj}^-, \Delta y_{mk}^-) \right] \quad (37)
\end{aligned}$$

where

$$g_{xy}^x(x, y) = \frac{\nu(\nu+1)}{\pi E} \left[\frac{y^2}{2} \log \left(\sqrt{x^2+y^2} + x \right) - \frac{1}{4}\sqrt{x^2+y^2} \left(\sqrt{x^2+y^2} + 2x \right) \right]. \quad (38)$$

All of these expressions may be found through direct iterated evaluation of the integrals, noting that as long as $n \neq m$ or $j \neq k$ the integrand (effectively the Green's function) is bounded, hence making Fubini's theorem applicable given the compactly supported domains of integration.

In the special case where $n = m$ and $j = k$, these formulae also hold. This fact is found by decomposing the integration domain to exclude the origin, for instance in the manner

$$\int_{-\Delta y/2}^{\Delta y/2} \int_{-\Delta x/2}^{\Delta x/2} \mathbf{dr} = \lim_{\varepsilon \rightarrow 0} \left(\int_{\varepsilon}^{\Delta y/2} + \int_{-\Delta y/2}^{\varepsilon} \right) \int_{\Delta x/2}^{\Delta x/2} \mathbf{dr}. \quad (39)$$

Since the antiderivatives of Eqs 30, 31, 32, 34, 36, and 38 all have well-defined limits with only removable discontinuities at the origin, integrals of the Green's functions defined through Eq. 39 all converge about the origin and the equations above also hold in the case where $n = m$ and $j = k$. These explicit expressions allow us to accurately evaluate $\mathbf{u}(\mathbf{r}_i)$ in $\Phi_{\text{data}}[\mathbf{f}]$.

Appendix C: Decay of displacement fields

Note that u_x and u_y are symmetric in form. Hence, it will suffice to prove just one of these assertions. Eq. 3 can be written as

$$\begin{aligned} u_x(\mathbf{r}) &= \frac{1+\nu}{\pi E} \int \frac{\mathbf{dr}}{|\mathbf{r}-\mathbf{r}'|} \left\{ \left[\frac{\nu(x-x')^2}{|\mathbf{r}-\mathbf{r}'|^2} + 1 - \nu \right] f_x(\mathbf{r}') + \nu \frac{(x-x')(y-y')}{|\mathbf{r}-\mathbf{r}'|^2} f_y(\mathbf{r}') \right\} \\ &\equiv \frac{1+\nu}{\pi E} \int \frac{\rho_x(\mathbf{r}, \mathbf{r}')}{|\mathbf{r}-\mathbf{r}'|} \mathbf{dr}' \end{aligned} \quad (40)$$

where $\rho_x(\mathbf{r}, \mathbf{r}')$ is $\mathcal{O}(1)$ as $|\mathbf{r}| \rightarrow \infty$. Without loss of generality, we assume that the coordinate system is centered at some point $\mathbf{0} \in \Omega$. The Euclidean distances can then be represented through the binomial expansion,

$$\frac{1}{|\mathbf{r}-\mathbf{r}'|^p} = \frac{1}{|\mathbf{r}|^p} \frac{1}{\left(1 - \frac{2\mathbf{r} \cdot \mathbf{r}'}{|\mathbf{r}|^2} + \frac{|\mathbf{r}'|^2}{|\mathbf{r}|^2}\right)^{p/2}} = \frac{1}{|\mathbf{r}|^p} \sum_{k=0}^{\infty} \binom{\frac{p}{2} + k - 1}{k} \left(\underbrace{\frac{2\mathbf{r} \cdot \mathbf{r}' - |\mathbf{r}'|^2}{|\mathbf{r}|^2}}_{\mathcal{O}(|\mathbf{r}|^{-1})} \right)^k. \quad (41)$$

Since $\mathbf{r} \notin \Omega$ and $\mathbf{r}' \in \Omega$, the series converges in the $|\mathbf{r}| \rightarrow \infty$ limit. Plugging this series into the last line of Eq. 40, where $p = 1$, one sees that in order to show that the magnitude of $u_x(\mathbf{r})$ is $\mathcal{O}(|\mathbf{r}|^{-q})$, it suffices to show that $\int \rho(\mathbf{r}, \mathbf{r}') \mathbf{dr}' \leq \mathcal{O}(|\mathbf{r}|^{-q+1})$.

Using the fact that $\int \mathbf{f}(\mathbf{r}) \mathbf{dr} = \mathbf{0}$, one finds that

$$\begin{aligned} \int \rho_x(\mathbf{r}, \mathbf{r}') \mathbf{dr}' &= \int (1-\nu) f_x(\mathbf{r}') \mathbf{dr}' + \nu \int \left[\frac{(x-x')^2}{|\mathbf{r}-\mathbf{r}'|^2} f_x(\mathbf{r}') + \frac{(x-x')(y-y')}{|\mathbf{r}-\mathbf{r}'|^2} f_y(\mathbf{r}') \right] \mathbf{dr}' \\ &= \frac{\nu}{|\mathbf{r}|^2} \int \left[(x-x')^2 f_x(\mathbf{r}') + (x-x')(y-y') f_y(\mathbf{r}') \right] \sum_{k=0}^{\infty} \left[\frac{2\mathbf{r} \cdot \mathbf{r}' - |\mathbf{r}'|^2}{|\mathbf{r}|^2} \right]^k \mathbf{dr}'. \end{aligned} \quad (42)$$

Expanding the leading order term of this expression, we see that

$$\begin{aligned} \int \rho_x(\mathbf{r}, \mathbf{r}') \mathbf{dr}' &= \frac{\nu}{|\mathbf{r}|^2} \int \left[(x-x')^2 f_x(\mathbf{r}') + (x-x')(y-y') f_y(\mathbf{r}') \right] \mathbf{dr}' \\ &= \frac{\nu}{|\mathbf{r}|^2} \left[-2x \int x' f_x(\mathbf{r}') \mathbf{dr}' + \int x'^2 f_x(\mathbf{r}') \mathbf{dr}' - x \int y' f_y(\mathbf{r}') \mathbf{dr}' - y \int x' f_y(\mathbf{r}') \mathbf{dr}' + \int x' y' f_y(\mathbf{r}') \mathbf{dr}' \right] \\ &= \mathcal{O}(|\mathbf{r}|^{-1}). \end{aligned}$$

Hence, it is evident that this integral is of $\mathcal{O}(|\mathbf{r}|^{-2})$, where to the leading order we have

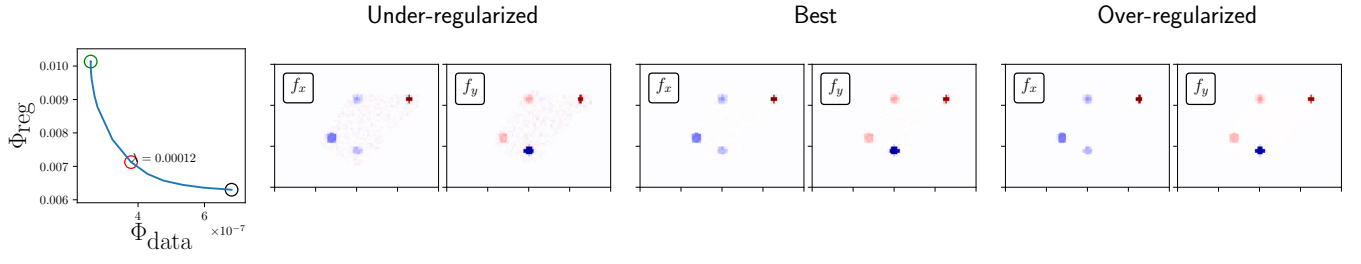


FIG. 11: **Choice of λ** by plotting the tradeoff between regularity and data mismatch.

$$\begin{aligned}
 u_x(\mathbf{r}) = & \frac{1+\nu}{\pi E |\mathbf{r}|^2} \left[-2\nu \frac{x}{|\mathbf{r}|} \int x' f_x(\mathbf{r}') d\mathbf{r}' - \frac{x\nu}{|\mathbf{r}|} \int y' f_y(\mathbf{r}') d\mathbf{r}' \right. \\
 & \left. - \frac{y\nu}{|\mathbf{r}|} \int x' f_y(\mathbf{r}') d\mathbf{r}' + (1-\nu) \frac{\mathbf{r}}{|\mathbf{r}|} \cdot \int \mathbf{r}' f_x(\mathbf{r}') d\mathbf{r}' \right] + \mathcal{O}(|\mathbf{r}|^{-3})
 \end{aligned} \tag{43}$$

Choice of regularization penalty parameter λ